In-depth quantitative analysis of the microstructures produced by Surface Mechanical Attrition Treatment (SMAT)

CrossMark

Y. Samih[a,b,*], B. Beausir[a,b], B. Bolle[a,b,c], T. Grosdidier[a,b,**]

[a]Université de Lorraine, Laboratoire d'Etude des Microstructures et de Mécanique des Matériaux (LEM3), CNRS UMR 7239, Metz F-57045, France
[b]Université de Lorraine, Laboratory of Excellence on Design of Alloy Metals for low-mAss Structures (DAMAS), Metz F-57045, France
[c]Ecole Nationale d'Ingénieurs de Metz, Laboratoire d'Etude des Microstructures et de Mécanique des Matériaux (LEM3), CNRS UMR 7239, Metz F-57045, France

ARTICLE DATA

ABSTRACT

Electron BackScattered Diffraction (EBSD) maps are used to characterize quantitatively the graded microstructure formed by Surface Mechanical Attrition Treatment (SMAT) and applied here to the 316L stainless steel. In particular, the analysis of GNDs – coupled with relevant and reliable criteria – was used to depict the thickness of each zone identified in the SMAT-affected layers: (i) the "ultrafine grain" (UFG) zone present at the extreme top surface, (ii), the "transition zone" where grains were fragmented under the heavy plastic deformation and, finally, (iii) the "deformed zone" where initial grains are simply deformed. The interest of this procedure is illustrated through the comparative analysis of the effect of some SMAT processing parameters (amplitude of vibration and treatment duration). The UFG and transition zones are more significantly modified than the overall affected thickness under our tested conditions.

1. Introduction

The Surface Mechanical Attrition Treatment (SMAT) [1,2] is a fairly recent technique for mechanical surface treatment. In this technique, a large number of balls are placed in a chamber and vibrated at high frequency by a generator. The sample to be treated, fixed at the upper side of the chamber, is impacted repeatedly by the flying balls so that its surface becomes heavily plastically deformed [1,2]. Beside its conventional use to harden the surface and improve its wear and fatigue properties [3,4], SMAT has also been used, for example, to activate the surface before nitriding [5–8] or to create multilayered laminate composites by subsequent roll bonding [9]. For all these potential applications, the metallurgical and microstructural states of the deformed surface have to be tailored in different ways and in a reproducible manner to form nanostructures and/or deep hardened zones.

* Correspondence to: Y. Samih, Université de Lorraine, Laboratoire d'Etude des Microstructures et de Mécanique des Matériaux (LEM3), CNRS UMR 7239, Metz F-57045, France. Tel.: +33 3 87 54 74 45; fax: +33 3 87 37 42 84.
** Correspondence to: T. Grosdidier, Université de Lorraine, Laboratoire d'Etude des Microstructures et de Mécanique des Matériaux (LEM3), CNRS UMR 7239, Metz, F-57045, France. Tel.: +33 3 87 31 54 08; fax: +33 3 87 37 42 84.
E-mail addresses: youssef.samih@univ-lorraine.fr (Y. Samih), Thierry.grosdidier@univ-lorraine.fr (T. Grosdidier).

As for severe plastic deformation processes, grain refinement of coarse-grained materials under SMAT involves various dislocation activities and the creation of subgrain boundaries. Even if the basic mechanisms of microstructure changes and nanostructuration [10,11] or plasticity of the surface [12–15] have been addressed by detailed investigations, the individual effect of the numerous processing parameters of SMAT still needs to be precisely quantified. These parameters are for example the size, the weight, the speed and the nature of the impacting balls, the duration of the treatment or the frequency and amplitude of the vibrating sonotrode. Thus, an efficient method for a quantitative description of the microstructure evolution under SMAT, that would enable to depict both rapidly and sufficiently accurately the effect of the processing parameters, has to be proposed. In the present work, raw orientation maps obtained by Electron BackScattered Diffraction (EBSD) are used to characterize the microstructures and general features of surfaces after SMAT with the direct goal of establishing an efficient procedure for quantifying the effect of the processing parameters.

2.   Materials and Experimental Methods

The material investigated in this study is the well documented 316L austenitic stainless steel (X2CrNiMo 18–14–3) with the following chemical composition: (wt.%) C: 0.017, Si: 0.38, P: 0.019, S < 0.002, Mn: 1.79, Mo: 2.74, Ni: 14.1, Cu: 0.16, Cr: 17.43 and Fe. The samples, 8 mm in thickness, were first mechanically polished to a mirror-like finish (1 μm diamond paste) and subjected to SMAT under an argon atmosphere in order to limit oxidation. A vibrating frequency of 20 kHz was selected for the generator to move 100Cr6-steel balls having a diameter of 1 mm. Four samples were treated using intercrossed variations of two parameters: the treatment duration (3 and 20 min) and the amplitude of the sonotrode (60 and 80 μm), all other conditions remaining similar. For clarity, the experimental conditions are summarized in Table 1.

The microstructure was analyzed using a Jeol 6500F Scanning Electron Microscope (SEM) with a Field Emission Gun (FEG). To investigate the affected depths after SMAT, the scans were obtained on cross sections perpendicular to the SMATed surfaces. Orientations were acquired by EBSD and treated with the Channel 5 system.

3.   Results and Discussion

3.1.   What Can Be Depicted?

The mechanisms of grain refinement for the 316L stainless steel have been detailed using Transmission Electron Microscopy (TEM) by Roland et al. [4,16]. At low strain, the microstructure is characterized by high density of mechanical twins and dislocation arrays. As the strain increases, twin–twin interactions occur which subdivide the original austenitic grains into smaller blocks and, ultimately, lead to the formation of randomly oriented nanocrystallites (50–400 nm) involving boundary sliding and rotation of crystalline domains. Consequently, SMAT produces gradients in grain size and structural defects through the depth below the surface. The magnitude of this gradient, which is directly related to the local strain sustained by the material, depends on the numerous processing parameters.

Fig. 1(A) gives a typical Band Contrast (BC) and Inverse Pole Figure (IPF) maps of the cross section of the 316L stainless steel after SMAT, recorded using a step size of 30 nm in the area of high strain regime below the surface. These maps are raw (not corrected) in which the black areas correspond to heavily strained regions, giving rise to blurred or overlapped Kikuchi patterns that could not be indexed. As shown in Fig. 1(A), at the bottom of the images (at the treated surface), the EBSD technique was not able to resolve the structure of a layer having a thickness of about 4 μm below the surface. Indeed, this area corresponds to the heavily deformed microstructure containing nanograins or domains having sizes as low as 20 nm [4,16] and, as a consequence, the indexing rate at different distances from the surface in this area is very low (always below 10%). Fig. 1(B) is an enlargement of the outlined red zone that shows that in this extreme surface layer, only few points were indexed (arrowed). As the distance from the surface increases, the indexing rate increases and the EBSD technique starts recording fine domains that clearly originate from grain and subgrain divisions. Most of these domains are highly misoriented. At a distance of about 6 μm from the surface (top of Fig. 1B), most of these domains still have a largely sub-micrometric size. As the distance from the interface further increases and the local strain decreases, it becomes easier to depict the presence of deformation twins (arrowed in the IPF map in Fig. 1A), as reported in [4,16].

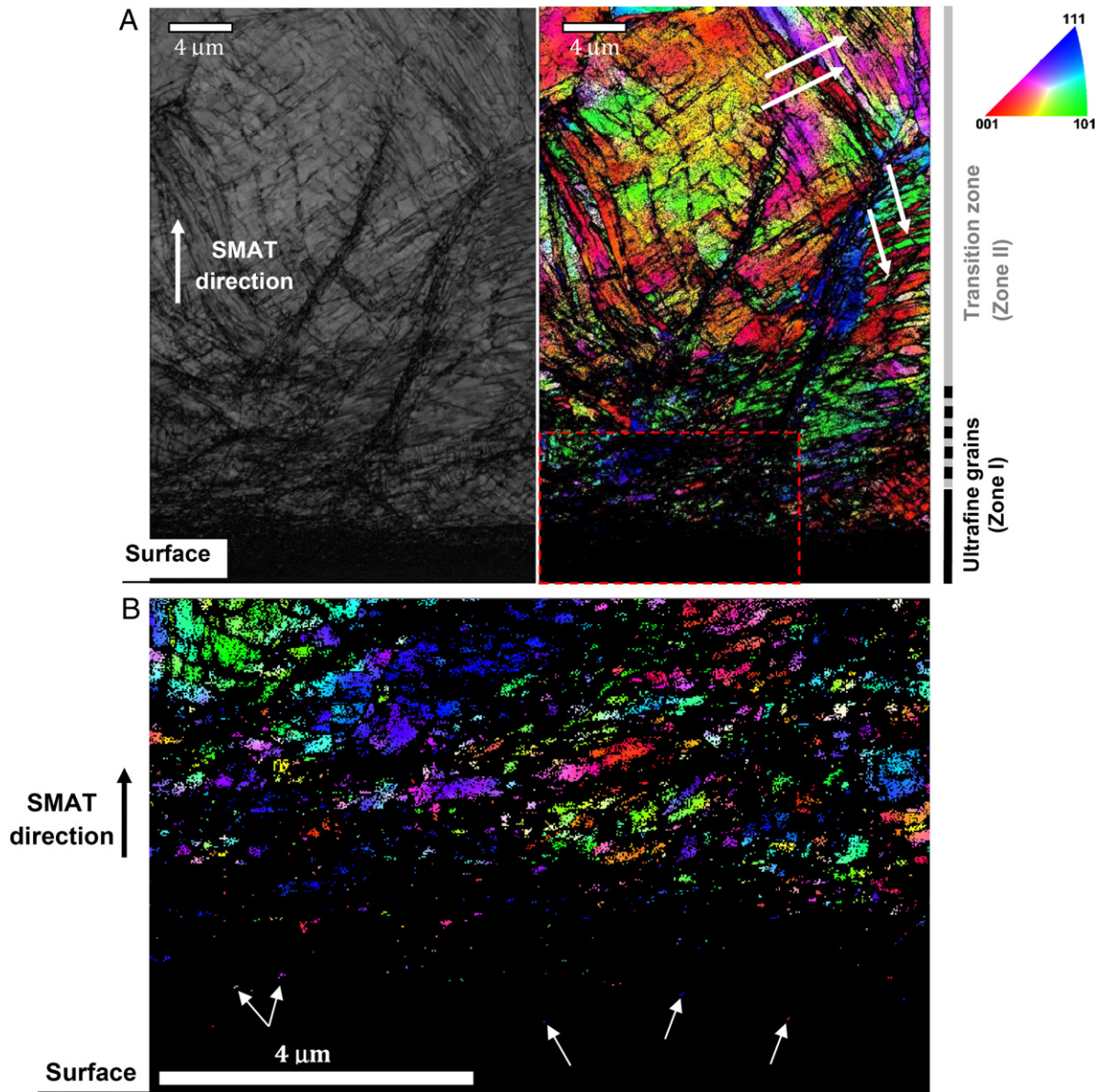| Table 1 – SMAT experimental conditions.								
	Balls				SMAT conditions			
Condition	Nature	Diameter (mm)	Number	Weight (g)	Amplitude of vibration (μm)	Treatment duration (min)	Vibrating frequency (kHz)	Distance sonotrode—sample (mm)	Atmosphere
1	100Cr6 steel	1	1800	7.6	60	3	20	30	Argon
2					80	20			
3					60	3			
4					80	20			

Fig. 1 – (A) Typical example of EBSD maps of the cross section obtained after SMAT with a very fine step size (30 nm) and (B) a close loop of the outlined zone in red. (For interpretation of the references to color in this figure legend, the reader is referred to the web version of this article.)

Fig. 2 gives more information concerning the misorientation degree within the microstructure in the same area. In the Band Contrast map in Fig. 2(A) are drawn in red lines corresponding to the Sigma-3 ((111) <60°>) twin boundaries. Consistent with the result of Roland et al. [4,16], a high density of deformation twins is observed. It is also clear that, even if the BC map is revealing long and thin deformation twins, the exact (111) <60°> twin boundary misorientation is generally not maintained over long distances. As suggested by the variation of shades of colors in the IPF map in Fig. 1(A), this is due to the accumulation of dislocations along the twin boundaries that creates a local misorientation gradient. For illustration, Fig. 2(B) and (C) presents the local accumulated misorientation relative to the first point following the two white arrows. In Fig. 2(B), a high number of Sigma-3 twin boundaries are detected and misorientation of

about 10° can be depicted in the matrix between the twin boundaries. In Fig. 2(C), closer to the surface where the level of strain sustained by the material is higher, in addition to a fewer number of Sigma-3 boundaries, broader and higher levels of accumulated misorientations are observed.

Clearly, this kind of high resolution EBSD map authorizes to depict the main features revealed by TEM concerning the grain refinement and associated deformation mechanisms. However, even if the analysis is much faster than a detailed TEM analysis, the drawback of such high resolution map is the necessary limitation of the covered surface if one wants to keep a reasonable duration of analysis (here, for this small map, about 8 h). Also, the statistical relevance of the observed phenomena may be questioned because the analyzed length on the surface remains of the order of the initial grain size
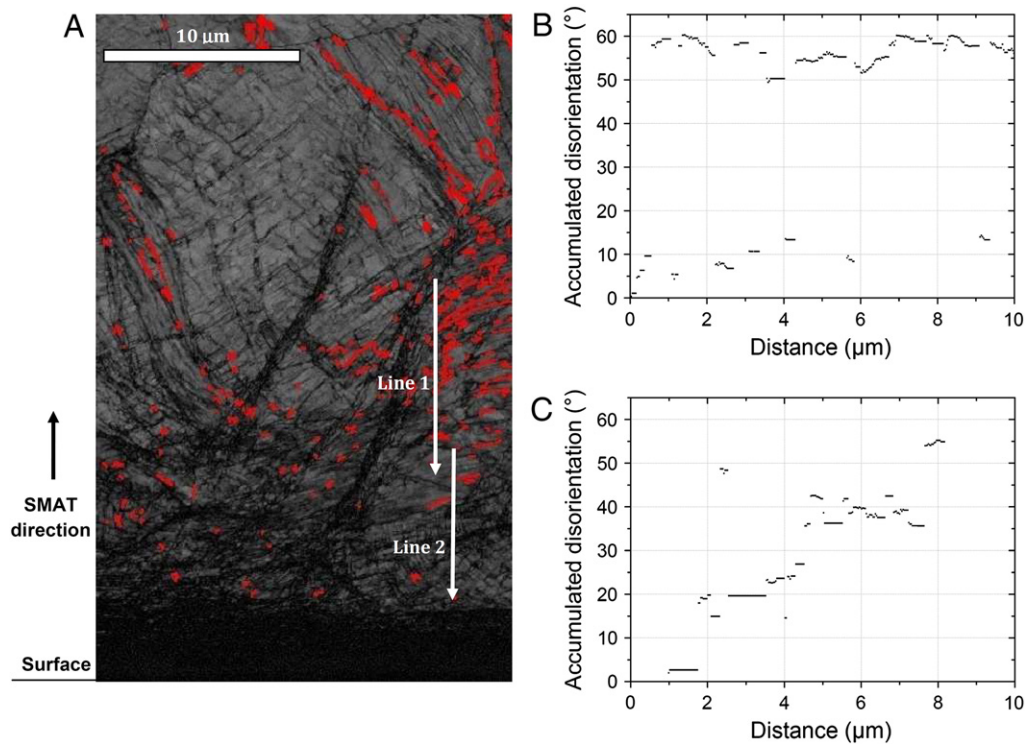
Fig. 2 – (A) The Sigma 3 twin boundaries (111) <60°> map (red lines) and the evolution of misorientation (B) in the subsurface and (C) at the top surface. (For interpretation of the references to color in this figure legend, the reader is referred to the web version of this article.)

(20 to 30 μm) and the depth of analysis is still restricted to about 40 μm, much below the depth of the area affected by the plasticity which may reach 200 μm [16,17]. However, it appears that it is possible to extract from EBSD maps relevant information on the plastic deformation induced by SMAT. It is then important to find other procedures of analysis using orientation maps to get a quantitative description of the level of plastic deformation imparted to the sample and, in consequence, determine the effect of the processing parameters.

Therefore, in the present work, information obtained from EBSD analyses are used to gain rapidly more insights on the microstructure evolution and to determinate the effectiveness of the processing parameters. In particular, it is important to be able to determine the thickness of the 3 different zones usually depicted in SMATed samples: (i) the so-called nano-crystalline domain, or more currently for metallurgists the domain of ultrafine grains having largely sub-micrometric sizes, that correspond to the ultimate stage of grain refinement under heavy deformation, (ii) the transition zone where the initial micrometric grains are fragmented under heavy deformation and (iii) the deformed zone where the initial grains are simply plastically deformed.

3.2. A Method to Characterize Efficiently SMATed Microstructures

This section describes how to use data obtained from EBSD to depict, more rapidly and in a quantitative way, the overall mesoscopic plastic strain gradients generated at the material subsurface by the SMAT treatment. In his pioneer paper

on non-homogeneous deformation, Ashby has introduced the distinction between statistically stored dislocations and geometrically necessary dislocations (GNDs) [18]. The GNDs accommodate the incompatibility of the elastic/plastic distortion, which arises only in the non-homogeneously deforming regions [18–20]. Thus, while the statistically stored dislocations – which develop in homogeneous deformation – have a predominant density at small strain, the amount of GNDs becomes more important at high strain and its local density is actually proportional to the rotational of the elastic/plastic distortion [19]. Therefore, by assuming that the loading during the SMAT is mainly compressive in nature, a good indicator of the plastic deformation imparted by the SMAT can be the distribution of the GND density as a function of the distance from the top treated surface. It is well established that the dislocation structure in a deformed material consists of cells, sub-gains and/or walls which accommodate the misorientations between dislocation-poor areas. This makes it possible to quantify the dislocation structure heterogeneity in deformed polycrystals by EBSD (see for example [21–23]). As the strain imparted to the material increases, the size of these domains decreases and the average misorientation between them increases. Consequently, as will be seen hereafter, this evolution can be depicted for SMATed sample by direct measurements of local misorientations at different depths using low magnification EBSD maps and the associated quantification of GND densities. However, at very high strain close to the surface, the ultimate stage of the deformation process under SMAT is the transformation of these domains in ultrafine grains having high angle grain boundaries within which dislocations are not stable anymore. In this

regime, the properties of the material are not any more GNDs-governed but more closely related to the grain size (Hall–Petch effect). Thus, this switching between different types of microstructure configurations requires other indicators for following the structure evolution in the vicinity of the surface where the highest strains were imparted. In this case, for which the indexing rate by EBSD decreases significantly, the apparent grain size will be used as the main criterion. The details of the procedure for depicting quantitatively the microstructure evolution is given hereafter and illustrated in Figs. 3 and 4.

By omitting the elastic deformation, a part of GND density can be extracted from orientation maps [25]. In the present work, raw orientation maps (without noise reduction) were used to extract the GND density according to the method proposed by Pantleon [25]. In order to quantify the GND densities only within the grains, the adjacent pixels across boundaries displaying a disorientation exceeding 5° were not considered in the calculation. Five components of the GND tensor (α), known also as the Nye tensor, can be determined from the 2D mappings [19,25]. Fig. 3(A) gives a map of the entry-wise norm of GND density tensor recorded with a step size of 200 nm. Note that for the sake of visual clarity, only the Band Contrast was plotted for densities smaller than 10% of the GND density maximum (see legend). In Fig. 3(B), the corresponding in-depth evolutions of GND density and indexation rate are given. It should be noted that the values of GND density are the average along each horizontal line parallel to the treated surface. At the bottom of Fig. 3(A), the top surface black layer for which the indexation rate is nearly 0 is present, as confirmed in Fig. 3(B). In this last figure, it can be seen that below this layer, the density of GNDs increases continuously to reach a maximum at about 50 μm. At this maximum of GND density, the indexation rate is now about 65%; the remaining 35% of non-indexed data points are due to the high strain and grain subdivision mechanisms taking place, which still result in blurred or overlapped Kikuchi patterns and appear as black dots in the map. As the depth increases further, the GND density starts decreasing and reaches the initial level of the bulk material at approximately 180 μm. The indexation rate within this zone continues to

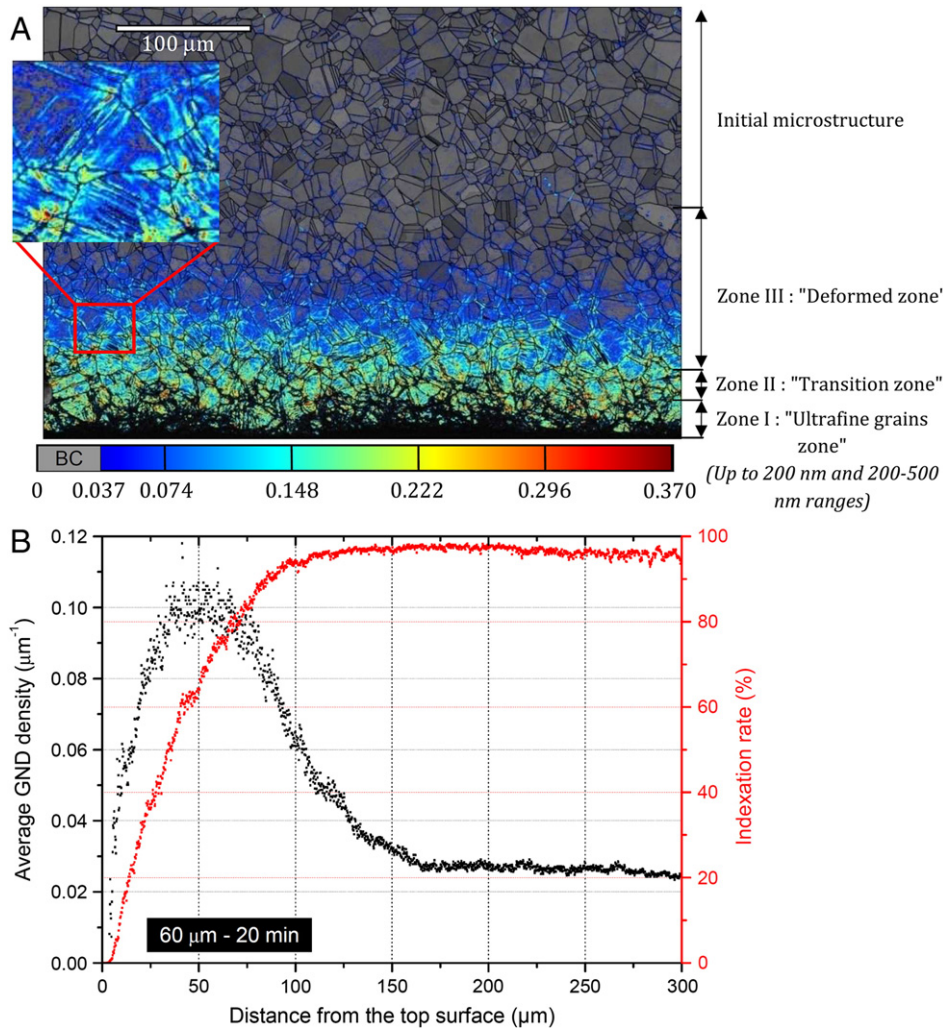

Fig. 3 – A) Map of GND density obtained from EBSD measurement in 316L stainless steel after 20 min SMAT with 60 μm vibrating amplitude. For intensities less than 0.037 μm^{-1} (bottom 10%), the Band Contrast (BC) was plotted. (B) The corresponding evolution of the average GND density (black dots) and the indexing rate (red dots) from the top surface. (For interpretation of the references to color in this figure legend, the reader is referred to the web version of this article.)
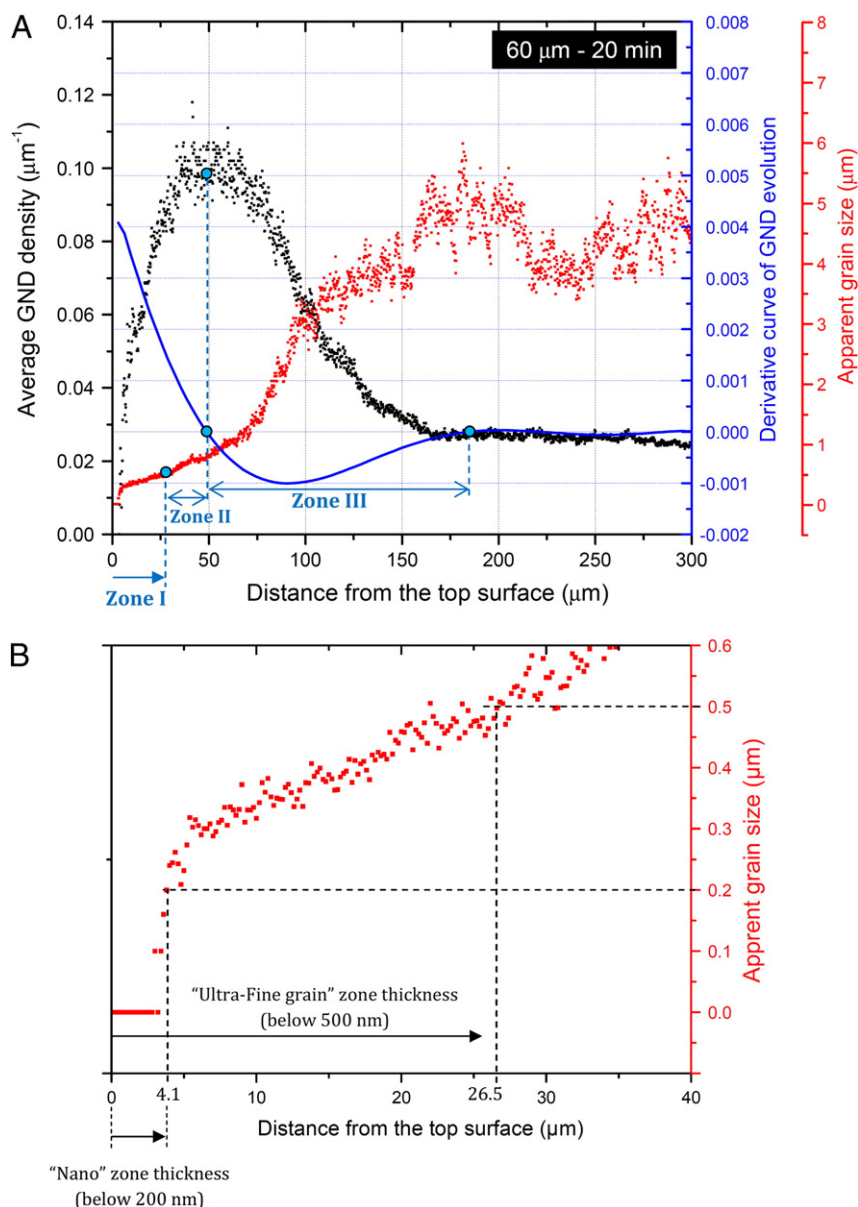
Fig. 4 – (A) Evolution of the average GND density (black dots), its derivative (blue dots) and the evolution of grain size (red dots), (B) zoom of the grain size evolution within the first 40 μm. (For interpretation of the references to color in this figure legend, the reader is referred to the web version of this article.)

increase and reaches a maximum of about 95%. The difficulty is thus to depict quantitatively using relevant and reliable criteria the thicknesses of the different domains. For this, several criteria were selected and represented in Fig. 4.

In Fig. 4(A), as a function of the distance from the top surface towards the bulk, the evolution of the average GND density (black dots) and, its derivative (solid blue line) and the evolution of the apparent grain size (red dots) obtained by the line intercept method along horizontal lines are plotted. The latter consists in placing a number of horizontal test lines (one line is placed on each pixel line along Y) on the EBSD map and counting the number of times a new grain boundary is intercepted. Using these three pieces of information, the thickness of the domains described before can be determined quite precisely.

The thickness of the UFG layer (Zone I) can be characterized by a corresponding grain size obtained by the line intercept method (red dots in Fig. 4). In a fairly arbitrary way, two equivalent grain sizes were selected here to characterize this domain: a "nano" range below 200 nm and another having an ultrafine grain size below 500 nm. These grain size ranges were fairly arbitrarily chosen because no conventional size range of the nano-crystalline domains is properly defined and a wide range of values are given in the literature. Using this criterion and Fig. 4(B), which is an enlargement of the apparent grain size evolution near the top surface, the thickness of this first "nano" zone below 200 nm is about 4 μm while the sub-500 nm domain reaches about 26.5 μm. The thickness of the "transition zone" (Zone II) can be depicted in Fig. 4(A) using the derivative of the GND density evolution. The derivative nullifies when the GND

density reaches the highest level, which corresponds to the end of the transition zone. Thus, the transition zone stretches approximately down to a depth of about 50 μm. Using these criteria, the thickness of this transition zone, where the grains are significantly fragmented by the heavy deformation but do not reach the ultrafine grain range, is therefore about (50–26.5 μm) 23.5 μm. Finally, going further within the depth of the material, the last characteristic zone – the deformed zone – (Zone III) is characterized by a continuous decrease of the GND density. The derivative curve in this zone is negative and nullifies when the GND density becomes low and constant in the unaffected zone, at about 183 μm. The thickness of this zone is then about (183–50 μm) 133 μm. In this zone, plastic deformation took place but the initial structure dominated by large grains is still visible. The apparent grain size, revealed by the line intercept method, changes in this domain because of the formation of a few deformation twins and the presence of dislocations creating a misorientation gradient. It is also important to recall here that, even if the size of the grains in the initial material is about 20 μm, the apparent grain size for the base material in Fig. 3(A) reaches a steady plateau at about 4.5 μm because of the presence of annealing twins that are counted as high angle boundaries in the automated analysis. The three so-obtained zones and their thicknesses are indicated in Fig. 3(A).

From this example, it is clear that large magnification EBSD maps coupled with the calculation of GND density can efficiently depict the main features of the different formed zones and mechanisms issued from grain fragmentation, twinning or dislocation activity revealed by detailed TEM investigations on the 316L stainless steel. Concerning the specific deformation of this steel, some comments need however to be made. First, as the deformation twins are often very fine [4], many of them are not directly depicted in the map with a step size of 200 nm. As sufficient amount of misorientation is generated by the plastic deformation along these twins, it is however possible to see them in the GND density map as shown in the enlargement (Fig. 3A) of the deformed zone. Second, it is also worth noting that the nucleation of strain induced martensitic variants at twin–twin boundaries previously reported in the 316L stainless steel treated by SMAT [4,16] was revealed in the present study by not only EBSD but also XRD and TEM.

The EBSD analysis would also be a powerful tool to depict such a strain induced martensitic transformation in steels or other materials [26,27]. The reason why the strain induced martensitic transformation was not depicted here is likely due to a much higher stability of the austenite in our alloy. Indeed, significant differences in terms of either the interstitial or substitutional alloying elements are authorized within the range of composition of the 316L stainless steel. These elements are classified as austenite-stabilizers or ferrite-stabilizers and their effect in this respect is often approximated using the following types of formulae [28]:

$$Ni_{eq} = Ni + Co + 0.5(Mn) + 30(C) + 0.3(Cu) + 25(N)wt.\% \quad (1)$$

$$C_{eq} = Cr + 2.0(Si) + 1.5(Mo) + 5.5(Al) + 1.75(Nb) + 1.5(Ti) \\ + 0.75(W)wt.\%. \quad (2)$$

Applied to the alloy treated by Roland et al. [16], this gives Ni_{eq} = 13.4 wt.% and Cr_{eq} = 20.9 wt.% while the values are Ni_{eq} = 15.5 wt.% and Cr_{eq} = 22.3 wt.% for the present alloy.

Whether the austenitic structure is sufficiently stable can also be described through the calculations of the Ms (Martensite-start) temperature as well as the M_{d30} temperature, the later corresponding to the temperature at which 50% of deformation induced martensite has formed for a true strain of 30%. These temperatures are calculated using the following equations [29,30]:

$$M_s(°C) = 502–810(C)–1230(N)–13(Mn)–12(Cr)–54(Cu)–6(Mo)wt.\% \quad (3)$$

$$M_{d30}(°C) = 497–462(C + N)–9.2(Si)–8.1(Mn)–20(Ni)–13.7(Cr) \quad (4) \\ –18.5(Mo)wt.\%.$$

Applied to the alloy treated by Roland et al. [16], these equations give value of M_s = –113 °C and M_{d30} = –39 °C. Comparatively, the alloy studied in the present work is characterized by much lower M_s (–192 °C) and M_{d30} (–100 °C) temperatures.

All these values indicate that a much lower driving force is required to trigger the deformation induced martensitic transformation in the case of the alloy studied by Roland et al. [16].

3.3. Application of the Procedure: Effect of Some Processing Parameters (Vibrating Amplitude and Treatment Duration)

Having established the above procedure based on the evolution of the GND distribution and apparent grain size to identify the different zones of the deformed material, it is now interesting to quantify the effect of some processing parameters. Fig. 5 shows the evolution of the GND density in four samples of the 316L stainless steel for which the vibration amplitude and treatment duration were varied. As it is well established that increasing the step size results in lowering the recorded GND density [24], all samples were analyzed using exactly the same procedure and step size (200 nm). To ease the comparison between the different samples, Fig. 6 compares the different estimated thicknesses of the different constitutional layers as well as the total affected zone.

A first striking feature revealed by this analysis is that the depth of the overall affected zones depends very little on the tested processing conditions. Indeed, the two samples treated under 60 μm amplitude as well as the one processed under 80 μm for the shortest time (3 min) have a rather close affected depth around 180 μm. Only a long treatment of 20 min at the highest amplitude (80 μm) increases the overall depth by about 20% (220 μm). Comparatively, the differences in the thicknesses of the UFG and transition zones are much more important and depend very much on the processing conditions (Fig. 6). The reason for this is that a certain amount of energy and sufficient times are required to authorize the combination of dislocation and the build-up of dislocation cells that will generate the microstructure evolution characterized by grain fragmentation and grain refining.

For the sample treated using the "softest" conditions (60 μm of vibration amplitude for 3 min), the so-called "ultra-fine grain"
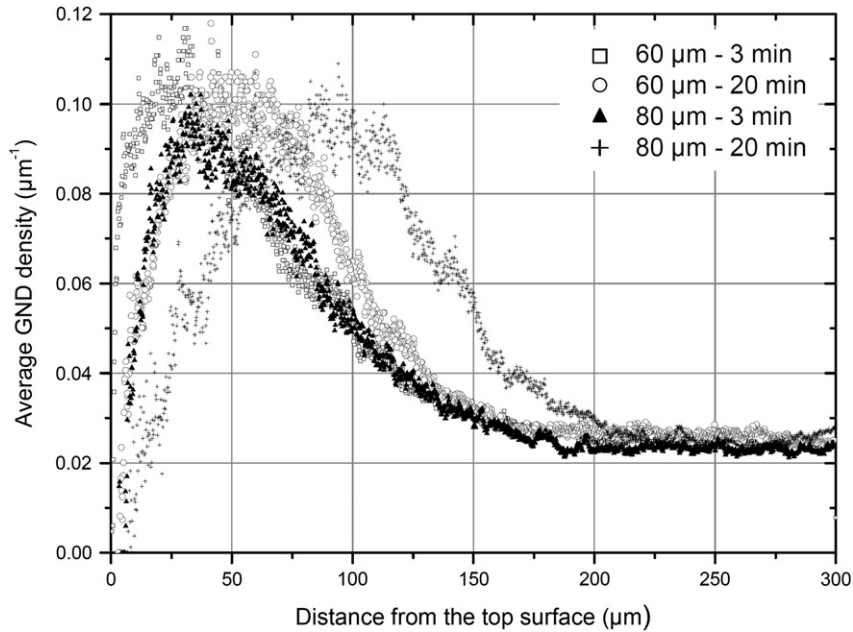
Fig. 5 – Evolution of the average GND density from the top surface to the bulk for different SMAT conditions.

domain corresponds to a 1.2 μm layer of sub-200 nm grains followed by a thickness of about 6.1 μm of grains in the 200–500 nm range. The thin size of the whole UFG layer (1.2 + 6.1 = 7.3 μm) indicates that the deformation imparted to the material did not lead to significant grain fragmentation. The subsequent transition zone has indeed a thickness of about 20 μm (19.7 μm), which leads to a total thickness of "fragmented" zone of 27 μm (7.3 + 19.7 = 23 μm) before reaching the so-called deformation zone.

Increasing the vibration amplitude to 80 μm for the same treating time of 3 min has a moderate effect on increasing the

depth of the total fragmented zone which reaches only 33 μm (6.4 + 13 + 13.6 = 33 μm). However, the higher vibration amplitude leads to a more advanced grain refinement process close to the surface. This leads to a total "ultra-fine grain" domain increased by almost a factor of 3 (19.4 μm versus 7.3 μm), and corresponding to a successive 6.4 μm + 13 μm thick layers of sub-200 nm and 200–500 nm grains, respectively.

As the grain fragmentation process requires a sufficiently high amount of multidirectional impacts, the increase in the treatment time from 3 to 20 min has a significant effect on the thicknesses of the UFG and transition zones within which the
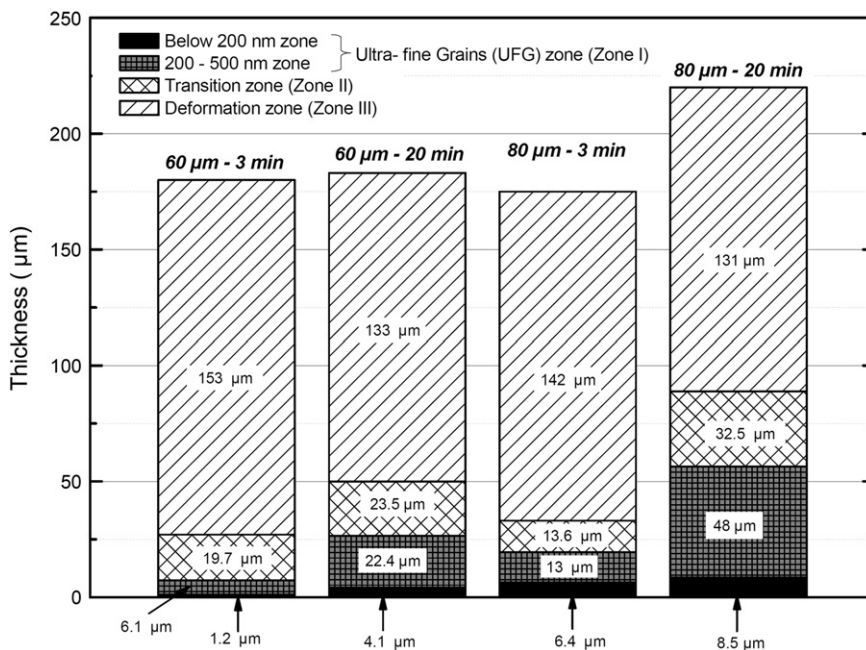

Fig. 6 – Thickness evolution of the different layers depending of the SMAT conditions for the 316L stainless steel.

Table 2 – Thickness (from the top surface) of the different types of microstructure layers.

Type of the affected domain	SMAT conditions			
	60 µm – 3 min	60 µm – 20 min	80 µm – 3 min	80 µm – 20 min
Overall affected zone (Zones I + II + III)	180 µm	183 µm	175 µm	220 µm
Total fragmented zone (Zones I + II)	27 µm	50 µm	33 µm	89 µm
'UFG' zones (Zone I)	7.3 µm	26.5 µm	19.4 µm	56.5 µm

(Multiplier factors indicated by arrows in the table: Overall affected zone: 175 → 220 ×1.2. Total fragmented zone: 27 → 50 ×1.8, 27 → 33 ×1.2, 33 → 89 ×1.8, 33 → 89 ×2.7. 'UFG' zones: 7.3 → 26.5 ×3.6, 7.3 → 19.4 ×2.7, 19.4 → 56.5 ×2.1, 19.4 → 56.5 ×2.9.)

combination of dislocations is the major driving mechanism. Indeed the thicknesses of the UFG domains are multiplied by a factor of about 3 or more while the overall fragmented domains increase by about 1.8 at 60 µm vibrating amplitude and about 2.7 under 80 µm. All the details are summarized in Table 2.

These examples clearly demonstrate the interest of the analyzing technique developed in the present work to correlate the SMAT parameters (amplitude and duration here) to the final deformed SMAT structure. Further work is now under way to investigate in a greater extent the relative effectiveness of a broader range of processing parameters on the microstructure evolution and grain refinement processes. We also believe that this type of approach – using the evolution of GND – should be helpful to quantitatively estimate the effectiveness of other treatments in which the SMAT process is used as a precursor prior to nitriding [31], co-rolling [32] or microarcing [33] as well as, more generally speaking, duplex treatments generating, on purpose, surface deformation gradients [34–36] or spatially heterogeneous microstructures [36–38].

4. Summary and Conclusions

Electron Backscattered Diffraction (EBSD) maps were used to characterize the deformed zones created by SMAT and applied here to determine the effectiveness of processing parameters on the 316L stainless steel.

High magnification maps with high resolution (step size of 30 nm) were used to reveal the grain refinement mechanisms encountered in this steel: the formation of twins and dislocation arrays leading to grain fragmentation followed by the final formation of largely sub-micrometric grains.

The degree of advancement of this refinement process obviously depends on the local strain sustained by the material and, consequently, creates gradients in grain size and amount of structural defects through the depth below the surface. The magnitude of these gradients depends on the processing parameters.

Low magnification maps (step size of 200 nm) were used to extract the GND density, which is a good indicator of the plastic deformation imparted by the SMAT treatment. The apparent grain size and the derivative of the GND density evolution were used to establish criteria allowing to depict quantitatively the thickness of the three zones present through the SMAT affected layer: (i) the "ultrafine grain (UFG)" zone having sustained high strain at the top surface, (ii) the sub-surface transition zone in which the extend of deformation is sufficient to activate grain sub-division of the initial grains and, finally, (iii) the deformed zone where the initial grains are simply plastically deformed.

This procedure was applied to compare the effect of two processing parameters: the vibration amplitude (60 and 80 µm) of the sonotrode and the treatment duration (3 and 20 min). It was noticed that the UFG and transition zone thicknesses are more significantly modified by these parameters than the overall affected layer one.

REFERENCES

[1] Liu G, Lu J, Lu K. Surface nanocrystallization of 316L stainless steel induced by ultrasonic shot peening. Mater Sci Eng 2000; A286:91–5.

[2] Lu K, Lu J. Nanostructured surface layer on metallic materials induced by surface mechanical attrition treatment. Mater Sci Eng 2004;A375–377:38–45.

[3] Wang ZB, Lu J, Lu K. Wear and corrosion properties of a low carbon steel processed by means of SMAT followed by lower temperature chromizing treatment. Surf Coat Technol 2006;201:2796–801.

[4] Roland T, Retraint D, Lu K, Lu J. Fatigue life improvement through surface nanostructuring of stainless steel by means of surface mechanical attrition treatment. Scr Mater 2006;54:1949–54.

[5] Tong WP, Tao NR, Wang ZB, Lu J, Lu K. Nitriding iron at lower temperatures. Science 2003;299:686–8.

[6] Tong WP, Liu CZ, Wang W, Tao NR, Wang ZB, Zuo L, et al. Gaseous nitriding of iron with a nanostructured surface layer. Scr Mater 2007;57:533–6.

[7] Lin YM, Lu J, Wang LP, Xu T, Xue QJ. Surface nanocrystallization by surface mechanical attrition treatment and its effect on stucture and properties of plasma nitrided AISI 312 stainless steel. Acta Mater 2006;54:5599–605.

[8] Panicaud B, Retraint D, Grosseau-Poussard JL, Li L, Guerain M, Goudeau P, et al. Experimental and numerical study of the effects of a nanocrystallisation treatment on high-temperature oxidation of a zirconium alloy. Corros Sci 2012;60:224–30.

[9] Waltz L, Retraint D, Roos A, Olier P. Combination of surface nanocrystallization and co-rolling: creating multilayer nanocrystalline composites. Scr Mater 2009;60:21–4.

[10] Zhang HW, Hei ZK, Liu G, Lu J, Lu K. Formation of nanostructured surface layer on AISI 304 stainless steel by means of surface mechanical attrition treatment. Acta Mater 2003;51:1871–81.

[11] Tao N, Zhang H, Lu J. Development of nanostructures in metallic materials with low stacking fault energies during surface mechanical attrition treatment (SMAT). Mater Trans 2003;44:1919–25.

[12] Micoulaut M, Mechkov S, Retraint D, Viot P, François M. Granular gases in mechanical engineering: on the origin of

heterogeneous ultrasonic shot peening. Granul Matter 2007;9: 25–33.

[13] Ruan HH, Chen AY, Chan HL, Lu J. Characterization of plastically graded nanostructured material: part I. The theories and the inverse algorithm of nanoindentation. Mech Mater 2010;42:698–708.

[14] Blonde R, Chan HM, Bonasso NA, Bolle B, Grosdidier T, Lu J. Evolution of texture and microstructure in pulsed electro-deposited Cu treated by Surface Mechanical Attrition Treatment (SMAT). J Alloys Compd 2010;504:S410–3.

[15] Zhang XC, Lu J, Shi SQ. A computational study of plastic deformation in AISI 304 induced by surface mechanical attrition treatment. Mech Adv Mater Struct 2011;18:572–7.

[16] Roland T, Retraint D, Lu K, Lu J. Enhanced mechanical behavior of a nanocrystallised stainless steel and its thermal stability. Mater Sci Eng, A 2007;445–446:281–8.

[17] Zhu KY, Vassel A, Brisset F, Lu K, Lu J. Nanostructure formation mechanism of α-titanium using SMAT. Acta Mater 2004;52:4101–10.

[18] Ashby MF. The deformation of plastically non-homogeneous materials. Phil Mag 1970;21:399–424.

[19] Nye JF. Some geometrical relations in dislocated crystals. Acta Metal 1953;1:153–62.

[20] Kröner E. Continuum theory of defects. In: Balian R, et al, editor. Physics of defects. Amsterdam: North Holland; 1980. p. 218–314.

[21] Field DP, Merriman CC, Allain-Bonasso N, Wagner F. Quantification of dislocation structure heterogeneity in deformed polycrystals by EBSD. Modell Simul Mater Sci Eng 2012;20: 024007.

[22] Dillien S, Seefeldt M, Allain S, Bouaziz O, Van Houtte P. EBSD study of the structure development with cold deformation of dual phase steel. Mater Sci Eng, A 2010;527:947–53.

[23] Beausir B, Fressengeas C. Disclination densities from EBSD orientation mapping. Int J Solids Struct 2013;50:137–45.

[24] Jiang J, Britton TB, Wilkinson AJ. Measurement of geometrically necessary dislocation density with high resolution electron backscatter diffraction: effects of detector binning and step size. Ultramicroscopy 2013;125:1–9.

[25] Pantleon W. Resolving the geometrically necessary dislocation content by conventional electron backscattering diffraction. Scr Mater 2008;58:994–7.

[26] Humbert M, Blaineau P, Germain L, Gey N. Electron backscattered diffraction study of epsilon/alpha′ martensitic variants induced by plastic deformation in 304 stainless steel. Metall Mater Trans A 2005;36A:3291–9.

[27] Germain L, Gey N, Humbert M, Hazotte A, Bocher P, Jahazi M. An automated method to analyze separately the microtextures of primary α_p grains and the secondary α_s inherited colonies in bimodal titanium alloys. Mater Charact 2005;54:216–22.

[28] Pickering FB. Physical metallurgical development of stainless steels. Proc Conf Stainless Steels 1984;84:2–28.

[29] Olson DL. Prediction of austenitic weld metal microstructure and properties. Weld Rec Suppl 1985;64–10:281S–95S.

[30] Sormail T. Precipitates in creep resistant austenitic stainless steels. Mater Sci Technol 2001;17:1–14.

[31] Chemkhi M, Retraint D, Roos A, Garnier C, Waltz L, Demangel C, et al. The effect of surface mechanical attrition treatment on low temperature plasma nitriding of an austenitic stainless steel. Surf Coatings Technol 2013;221:191–5.

[32] Waltz L, Retraint D, Roos A, Garnier C, Olier P. Effect of interfacial oxidation occurring during the duplex process combining surface nanocrystallisation and co-rolling. Surf Coat Technol 2011;205:4608–13.

[33] Wen L, Wang YM, Liu Y, Zhou Y, Guo LX, Ouyang JH, et al. EIS study of a self-repairing oxidation coating. Corros Sci 2011;618:623–53.

[34] Zou JX, Zhang KM. Formation of ultrafine austenite on a cold rolled 316L stainless steel induced by pulsed electron beam treatment under heating mode. Thin Solid Films 2012;526: 28–33.

[35] Grosdider T, Zou JX, Stein N, Boulanger C, Hao SZ, Dong C. Texture modification, grain refinement and improved hardness/corrosion balance of a FeAl alloy by pulsed electron beam surface treatment in the heating mode. Scr Mater 2008;58:1058–61.

[36] Kamikawa N, Huang X, Hansen N. Tailoring structures through two-step annealing process in nanostructured aluminum produced by accumulative roll-bonding. J Mater Sci 2008;43:7313–9.

[37] Grosdidier T, Goran D, Llorca Ji G. On the processing of hetero-nanostructured metals for improved strength/ductility balance by ECAE and SPS techniques. J Alloys Compd 2010;504S:S456–9.

[38] Witkin D, Lee Z, Rodriguez R, Nutt S, Laverina E. Al–Mg alloy engineered with bimodal grain size for high strength and increases ductility. Scr Mater 2003;49:297–302.